Research Square

Preprints are preliminary reports that have not undergone peer review.
They should not be considered conclusive, used to inform clinical practice,
or referenced by the media as validated information.

A minimal Asgard archaeal ESCRT-III system remodels membranes across scales

Henry Zivkovic
https://orcid.org/0009-0006-1410-7177
Dominik Hrebik
Max Planck Institute for Biochemistry
Béla Frohn
AITHYRA https://orcid.org/0000-0003-3067-9184
Jérôme Basquin
Max Planck Institute for Biochemistry
Margot Riggi
Max Planck Institute for Biochemistry
John Briggs
Max Planck Institute of Biochemistry https://orcid.org/0000-0003-3990-6910
Petra Schwille
schwille@biochem.mpg.de
Max Planck Institute of Biochemistry https://orcid.org/0000-0002-6106-4847

Article

Keywords:

Posted Date: August 28th, 2026

DOI: https://doi.org/10.21203/rs.3.rs-10742307/v1

License: This work is licensed under a Creative Commons Attribution 4.0 International License.
Read Full License

Additional Declarations: There is **NO** Competing Interest.

Abstract

Cells remodel membranes across spatial scales, from cell division to nanoscale scission. In eukaryotes, ESCRT-III/Vps4 machineries remodel endosomal membranes and narrow membrane necks using expanded ESCRT-III repertoires, including twelve ESCRT-III-related proteins in humans. By contrast, many Asgard archaea, the closest known archaeal relatives of eukaryotes, encode only two ESCRT-III subunits and Vps4. Whether such minimal systems retain nanoscale ESCRT-like remodelling and support larger-scale membrane organization remains unknown.

Here, we reconstitute the Lokiarchaeal ESCRT-III/Vps4 system and show that it couples distinct assembly modes across scales. ESCRT-IIIA forms micron-scale filaments and rings that constrict and disassemble upon Vps4 addition, whereas ESCRT-IIIB forms tens-of-nanometres spirals that Vps4 condenses. Together, the subunits co-assemble into spring-like polymers that are selectively remodelled by Vps4. On free-standing membranes, the complete machinery deforms and constricts multi-micron vesicles.

Thus, a two-subunit archaeal ESCRT-III/Vps4 system preserves eukaryotic-like polymerization and Vps4 regulation while enabling unexpectedly versatile membrane remodelling across scales.

Main

Membrane remodelling is essential for cellular life. Cells must bend, constrict and sever lipid bilayers during processes such as division, trafficking, repair and compartment formation, while preserving membrane integrity[1–3]. These transformations are driven by protein machineries that convert molecular-scale interactions with lipids into membrane deformation across many orders of magnitude[4]. How such machineries evolved, and how much molecular complexity is required to generate regulated membrane shape changes, remain central questions in cell biology.

In eukaryotes, many membrane-budding and scission reactions are mediated by the Endosomal Sorting Complex Required for Transport (ESCRT) machinery5[5–7]. In the canonical endosomal pathway, ESCRT-0 recognizes and concentrates ubiquitinated cargo, ESCRT-I and ESCRT-II facilitate cargo sorting, and ESCRT-II promotes recruitment and nucleation of ESCRT-III[8–10]. ESCRT-III then assembles into membrane-bound polymers that drive membrane deformation, constriction and scission, while the AAA ATPase Vps4 remodels and recycles ESCRT-III subunits[11]. Thus, ESCRT-III/Vps4 forms the core membrane-remodelling module of a broader trafficking pathway. Beyond endosomal sorting, ESCRT-III-dependent membrane remodelling also contributes to viral budding, plasma membrane repair, nuclear envelope repair and cytokinetic abscission[12–15]. Although ESCRT-III can be recruited to large cellular structures, membrane scission is generally executed at narrow membrane necks, highlighting the importance of nanoscale polymer organization in canonical eukaryotic ESCRT function[16–18].

Homologues of ESCRT-III proteins and Vps4 are also found in archaea[19]. In contrast to eukaryotes, archaeal ESCRT-like systems generally lack the full ESCRT-0, ESCRT-I and ESCRT-II pathway, but retain at least ESCRT-III and Vps4 homologues[19–21]. These reduced systems reveal which membrane-remodelling activities are intrinsic to the ESCRT-III/Vps4 module. This question is particularly relevant for Asgard archaea, the closest known archaeal relatives of eukaryotes, which encode simplified ESCRT systems that may illuminate the evolutionary origins of eukaryotic membrane-remodelling machineries[19,21,22]. Many Asgard genomes encode only two ESCRT-III homologues together with Vps4, raising the question of whether such minimal systems can reproduce key features of eukaryotic ESCRT function, including membrane-dependent polymerization, ordered co-assembly and ATPase-dependent remodelling.

Recent studies have begun to reveal the structural and functional diversity of archaeal ESCRT-like systems. Heimdallarchaeal ESCRT-III proteins assemble into membrane-associated arrays or tubes[23], Lokiarchaeal ESCRT-III proteins can form nucleic-acid-associated filaments and helical rods[24], and Asgard Vps4 can partially complement loss of Vps4 in yeast[25].

In crenarchaea such as *Sulfolobus acidocaldarius*, ESCRT-like Cdv proteins form micron-scale rings that constrict during cell division[26–29]. These observations indicate that ESCRT-like polymers are not intrinsically limited to nanoscale membrane necks and may bridge molecular and cellular length scales. However, it remains unclear whether a minimal Asgard ESCRT-III/Vps4 system is sufficient to assemble on membranes, generate structures across multiple spatial scales and undergo selective ATPase-dependent remodelling.

Here, we reconstituted the ESCRT-III and Vps4 homologues from the Asgard archaeon Candidatus Lokiarchaeum on model membranes[20]. By isolating this minimal ESCRT-III/Vps4 system, we specifically explored whether and how functional specialization and regulated membrane remodelling could emerge from only two ESCRT-III subunits and one ATPase.

Results

Phylogenetic placement and predicted structural features of Lokiarchaeal ESCRT-III proteins

Phylogenetic analysis places the two Lokiarchaeal ESCRT-III homologs, ESCRT-IIIA and ESCRT-IIIB, within the ESCRT-III “early” and “late” functional groups, respectively (Supplementary Fig. 1a)[10,23,30]. Secondary-structure predictions indicated that both proteins retain the conserved five-helix ESCRT-III core, supporting their assignment as bona fide ESCRT-III family members (Supplementary Figs. 1 and 2a,b). As observed in other Asgard archaeal ESCRT-III systems, the two subunits differ mainly in their N-terminal h0 and C-terminal h6 regions (Supplementary Figs. 1 and 2a,b), suggesting functional specialization rather than redundancy.

The predicted h0 region of ESCRT-IIIA is enriched in positively charged residues and appears largely unstructured, whereas the h0 region of ESCRT-IIIB forms an amphipathic α-helix commonly associated with membrane interaction (Supplementary Figs. 1 and 3a,b)[31]. At the C terminus, both proteins contain a structured amphipathic h6 helix resembling a MIM1-like Vps4-interaction motif (Supplementary Fig. 4a,b)[32,33]. ESCRT-IIIA also contains a predicted MIM2-like motif, a feature associated with stronger Vps4 binding in eukaryotic ESCRT-III proteins such as Snf7/CHMP4 (Supplementary Fig. 4a)[34]. Yeast ESCRT-III proteins containing MIM1 and MIM2 motifs are differentially regulated by Vps4, with MIM2 promoting removal of early assembly subunits and MIM1-containing proteins mediating membrane scission[10,32,34]. This raises the possibility that ESCRT-IIIA assemble before ESCRT-IIIB *in vivo*, and that Vps4 regulates ESCRT-IIIA and ESCRT-IIIB in a subunit-specific manner.

ESCRT-IIIA assembles into micron-scale membrane-bound filaments and rings

We recombinantly expressed and purified Lokiarchaeal ESCRT-IIIA (CHMP4-7; Lokiarch_16760), ESCRT-IIIB (CHMP1-3; Lokiarch_37480), and Vps4 in *E. coli* BL21 as N-terminal His–Trx fusion proteins (Supplementary Fig. 5). As both ESCRT-III proteins lack cysteine residues, we introduced single cysteines at their C-termini to enable site-specific fluorescent labelling. Using Dynamic light scattering (DLS), we determined that both ESCRT-IIIA and ESCRT-IIIB exhibited hydrodynamic radii consistent with monomers in solution (Supplementary Fig. 6a), consistent with the closed soluble state described for other ESCRT-III proteins.

Because the source organism is uncultured, we characterized Vps4 activity to define assay conditions. ATP hydrolysis was maximal at pH 7.5 and 42.5°C (Supplementary Fig. 6b), but subsequent experiments were performed at pH 7.5 and room temperature (23 ± 1°C) to slow Vps4-dependent processes. Thermal unfolding confirmed protein stability under these conditions (Supplementary Fig. 6c).

We next reconstituted fluorescently labelled ESCRT-IIIA on supported lipid bilayers (SLBs) to study their behaviour by fluorescence confocal microscopy. Because eukaryotic and Heimdall archaeal ESCRT-III proteins are known to require negatively charged membranes to bind, we compared protein behaviors on neutral (DOPC:DOPE-ATTO655; 99.95:0.05 mol%) or anionic membranes (DOPC:DOPS:DOPE-ATTO655; 59.95:40:0.05 mol%). Both ESCRT-IIIA and ESCRT-IIIB only associated stably with membranes containing 40 mol% DOPS (Supplementary Fig. 7a,b).

Timelapse confocal imaging revealed that individual filaments elongate unidirectionally from distinct nucleation points and curl clockwise during growth (92 of 92 filaments analyzed; Fig. 1a,k; Supplementary Fig. 6d, MovieS1). This chiral growth behaviour resembles FtsZ filaments, in which filament polarity, intrinsic curvature and membrane binding together drive directional growth[36]. Below 2 μM, only sparse punctae binding sites were observed (Supplementary Fig. 7c). At 2 μM, single curved filaments frequently appeared and grew into rings with a mean diameter of 0.96 ± 0.17 μm (n = 191;

Fig. 1b,c,k). At higher membrane coverage, many filaments originated from one nucleation point, resulting in star-like structures with consistently curved beams (Fig. 1d,k). The formation of approximately 1-µm-diameter rings (Fig. 1b), suggests that ESCRT-IIIA behaves as a semiflexible polymer with a persistence length on the order of the ring radius, comparable to that of *E.coli* FtsZ filaments, involved in cell division[37,38].

We found that ESCRT-IIIA-Alexa488 formed dense networks of microns-long filaments at 3 µM (Fig. 1d,k; Movie S2). Notably, the fluorescent lipid dye DOPE-ATTO655 was excluded from regions beneath ESCRT-IIIA assemblies (Fig. 1e,f,g: MovieS3), suggesting local alteration of membrane properties upon filament binding.

Atomic force microscopy (AFM) provided additional structural information. The thinnest filaments we observed were curved and 4 nm in height (Fig. 1h). Further analysis showed that bundled filament widths occurred in discrete multiples (Supplementary Fig. 6e,f). Our observations are consistent with single filaments able to laterally interact to form increasingly thicker and straighter assemblies (Fig. 1h; Supplementary Fig. 6e,f). We frequently saw branching events at junctions between straight bundles and curved filaments, occasionally at near-orthogonal angles (Fig. 1h).

To further resolve filament architecture, we examined ESCRT-IIIA assemblies by cryo-electron microscopy (cryo-EM) on lipid monolayers of the same lipid composition. Cryo-EM micrographs also displayed single filaments and filament bundles (Fig. 1i). 2D class averages show single filaments and double filament structures with or without intrinsic curvature (Fig. 1i,j). Together, AFM and cryo-EM revealed flexible ESCRT-IIIA filaments with lower curvatures than ESCRT-III-like homopolymers such as Vipp1, Snf7 or CHMP4B[39–41].

Together, our results demonstrate ESCRT-IIIA shows expected ESCRT-III membrane-binding behavior, but the phenomenology of the resulting filaments differs strongly from those of eukaryotic ESCRT-III. The polymerization into micron-long filaments and rings exceeds known canonical ESCRT-III scales. Additionally, it shows branching and bundling abilities that are usually found in other protein families responsible for large-scale membrane transformations or cell-shape integrity.

Vps4 disassembles ESCRT-IIIA assemblies in an ATP-dependent manner

Since the observed ring structures of ESCRT-IIIA filaments were large enough to resolve by light microscopy, we next asked whether Vps4-dependent remodelling could be followed in real time. Indeed, when adding Vps4 in the presence of ATP, filament fluorescence intensity decreased over time, accompanied by the appearance of bright puncta at former assembly sites (Fig. 2a-c). By contrast, no changes occurred in the absence of ATP (Fig. 2b), demonstrating that ESCRT-IIIA remodelling requires Vps4 ATPase activity.

At higher magnification, Vps4 treatment led to processive shortening of filaments without internal breakage and symmetric gradual constriction of ESCRT-IIIA rings (Fig. 2c,d). This suggests filament tips are favorable to Vps4-mediated regulation (Fig. 2c,d, MovieS4). Upon prolonged incubation times, most filamentous structures were lost, leaving residual ESCRT-IIIA signal at former assembly sites (Supplementary Fig. 7d). In parallel, the membrane fluorescence recovered a homogeneous distribution, reflecting the removal of ESCRT-IIIA as a functional membrane shaping polymer (Fig. 2e,f; Supplementary Fig. 7d).

AFM imaging after Vps4 treatment confirmed efficient disassembly of ordered ESCRT-IIIA polymers, leaving sparse residual features instead (Fig. 1h, 2g). In Vps4-treated samples, our cryo-EM acquisitions revealed a loss of ordered protofilament architecture, with large pools of unstructured protein and fragmented filament-like remnants (Fig. 2h).

These experiments demonstrate that the AAA ATPase Vps4 remodels ESCRT-IIIA assemblies in an ATP-dependent manner, constricting rings and depolymerizing filaments despite their unusually large scale.

ESCRT-IIIB assembles into spiral arrays on membranes

We added fluorescently labelled ESCRT-IIIB to SLBs under the same conditions used for ESCRT-IIIA. In contrast to ESCRT-IIIA, ESCRT-IIIB associated broadly with membranes containing anionic lipids and appeared as a continuous protein layer at optical resolution rather than discrete large-scale assemblies (Fig. 3a; Supplementary Fig. 7b). Increasing the ESCRT-IIIB concentration from 500 nM to 2 µM did not promote a concentration-dependent transition to micron-scale filament networks as observed for ESCRT-IIIA (Supplementary Fig. 8a).

Below optical resolution however, AFM imaging revealed that this apparently diffuse membrane signal corresponded to organized nanoscale assemblies rather than a uniform protein coat. Intriguingly, ESCRT-IIIB formed circular filament arrays with central openings (Fig. 3b,c). Further analysis indicated that these in fact correspond to spirals with a varying number of turns, ranging from single to multiple turns (Fig. 3c,d). We measured a mean inner diameter of 13.8 ± 2.7 nm (s.d.; n = 30). Individual curved filaments were occasionally observed at the periphery of spiral structures, consistent with Snf7 spiral growth intermediates observed by Chiaruttini *et al.* (Fig. 3c)[40,42].

Spiral assemblies are a distinctive hallmark of ESCRT-III polymerization. Thus, despite its phylogenetic placement within the late ESCRT-III group, ESCRT-IIIB forms membrane-bound polymers that are morphologically reminiscent of canonical Snf7 spirals.

Vps4 binds and condenses ESCRT-IIIB spiral assemblies

To test the effect of Vps4 on ESCRT-IIIB assemblies, pre-assembled ESCRT-IIIB–Alexa565 structures were washed to remove unbound protein and then incubated with unlabelled Vps4 in the presence of

ATP. Immediately after Vps4 addition, ESCRT-IIIB fluorescence intensity increased, followed by the appearance of bright puncta co-localized with the membrane channel (Fig. 3e,f). Unlike ESCRT-IIIA, ESCRT-IIIB was not removed from the membrane upon Vps4 treatment (Fig. 3e,f).

AFM imaging showed that Vps4 led to a condensation of ESCRT-IIIB spirals (Fig. 3g). Small densities with heights consistent with Vps4 hexamers appeared on the condensed spirals. Height profiles confirmed that the hole diameters decreased and suggest a tighter overall packing of the filaments, explaining the apparent increase in fluorescence previously observed (Fig. 3g,h).

Cryo-EM further supported this conclusion. Whereas ESCRT-IIIB spirals were too heterogeneous to yield robust 2D class averages in the absence of Vps4, Vps4 promoted a more regular organization of ESCRT-IIIB spirals on lipid monolayers, readily visible in raw micrographs (Fig. 3i; Supplementary Fig. 8c). We measured 2D class averages of Vps4 hexameric particles, resulting in a diameter of ~ 13.0 nm, consistent with AlphaFold2 predictions (measured at 13 nm), DLS measurements (13.0 ± s.d. 1.8 nm; n = 23) and reported values for eukaryotic Vps4 (Supplementary Fig. 6a)[35]. 2D class averages contained Vps4 particles predominantly localized at spiral edges, where the average ESCRT-IIIB inter-filament distance was 3.24 ± 0.08 nm (s.d.; n = 9, Fig. 3h; Supplementary Fig. 9). Snf7 interfilament distances were averaged at 14 nm by Jukic *et al.*, a comparably very loose structure[40].

Together, these data reveal that Vps4 differently regulates the two Lokiarchaeal ESCRT-III subunits. Consistent with their distinct predicted Vps4-interaction motifs, ESCRT-IIIA is disassembled by Vps4, whereas ESCRT-IIIB remains membrane-associated and is condensed into compact spirals.

ESCRT-IIIA and ESCRT-IIIB co-assemble into higher-order polymers

Because ESCRT-III function commonly depends on heteropolymer formation, ESCRT-IIIA and ESCRT-IIIB were added sequentially to SLBs in both possible orders. When we added ESCRT-IIIA-488 to membranes pre-coated with ESCRT-IIIB-565, ESCRT-IIIA bound uniformly and masked the underlying ESCRT-IIIB signal (Supplementary Fig. 8b). Under these conditions, the characteristic rings and long filaments formed by ESCRT-IIIA alone were not observed.

In the reciprocal order, that is, the canonical homologous eukaryotic order[10], ESCRT-IIIA was first allowed to assemble into membrane-bound filaments and rings, followed by addition of ESCRT-IIIB–Alexa565 (Fig. 4a). ESCRT-IIIB strongly co-localized with pre-existing ESCRT-IIIA structures, a characteristic ESCRT-III behavior demonstrated in other systems[9,10] (Fig. 4a,b). Although ESCRT-IIIB continued to bind free membrane, its fluorescence intensity was markedly higher on ESCRT-IIIA assemblies, indicating a favorable recruitment to ESCRT-IIIA (Fig. 4a,b).

Upon co-reconstitution of both ESCRT-III proteins on lipid monolayers, cryo-EM not only revealed the formation of higher-order filamentous structures, but also the abolishing of homopolymeric phenotypes

observed in single-protein experiments. In the ESCRT-IIIA-B order of assembly, long spring-like helical filaments (approximately 460 nm in Fig. 4c) appeared with a consistent diameter of 27.9 ± 0.2 nm (s.d.; n = 9) and a variable pitch of 8.4 ± 0.2 nm (s.d.; n = 9; Fig. 4c,f). The helical filaments lacked continuous membrane contact but were only observed in the presence of lipid substrates, a primary ESCRT-III assembly requirement.

When we added ESCRT-IIIB prior to -IIIA (ESCRT-IIIB-A order), cryo-EM grids abundantly contained heterogeneous circular structures, possibly representing incomplete or uncoiled assembly products (Fig. 4d).

Our data show ESCRT-IIIA and ESCRT-IIIB cooperatively form new assemblies in a sequence-dependent manner, conceptually similar to canonical ESCRT-III proteins. Strikingly, the horizontal orientation of the spring-like polymers on the membrane is a major difference with other ESCRT-III systems, providing a route to access larger-scale membrane organization.

Vps4 remodells ESCRT-IIIA/IIIB assemblies

The effect of Vps4 on polymeric ESCRT-IIIA/-IIIB (canonical order) assemblies was first examined after washing unbound protein from the fluorescence microscopy assays. Addition of Vps4 and ATP resulted in an immediate increase in ESCRT-IIIB fluorescence intensity, followed by the appearance of bright aggregates containing both proteins (Fig. 4e). The ESCRT-IIIB signal remained overall intact, whereas the ESCRT-IIIA signal significantly decreased (Fig. 4e). These observations suggest the individual subunit-specific regulation by Vps4 is retained for co-dependent assemblies.

Cryo-EM confirmed that Vps4 disrupted the ordered helical architecture of the spring-like assemblies. In treated samples, regular spring-like filaments were replaced by disorganized protein assemblies and elongated dense filaments of approximately 30 nm in width, which lacked clear periodicity (Fig. 4g).

In conclusion, we find that Vps4 removes ESCRT-IIIA and condenses ESCRT-IIIB even when co-dependently assembled. The remaining features are long and dense filamentous structures containing principally ESCRT-IIIB. Having reconstituted the complete ESCRT-III/Vps4 machinery, we next asked whether it could remodel free-standing membranes.

The Lokiarchaeal ESCRT-III machinery deforms free-standing membranes

To test whether the Lokiarchaeal ESCRT-III machinery can remodel membranes at larger spatial scales, we reconstituted ESCRT-IIIA–Alexa488, ESCRT-IIIB–Alexa565 and unlabelled Vps4 on giant unilamellar vesicles (GUVs). ESCRT-IIIA bound to GUV membranes and polymerized into micron-long filaments, similar to those observed on SLBs (Fig. 5a). Subsequent addition of ESCRT-IIIB led to strong colocalization with ESCRT-IIIA and the membrane (Fig. 5b).

In addition to this recruitment behaviour, ESCRT-IIIA/IIIB assemblies locally deformed the GUV membrane into structures resembling braided membrane–protein assemblies in fluorescence images (Fig. 5b). This indicates that the mixed ESCRT-III polymers can reorganize free-standing membranes, rather than only assembling on supported bilayers. Upon addition of Vps4 and ATP, GUVs underwent constriction while ESCRT-IIIA, ESCRT-IIIB and membrane signals remained colocalized (Fig. 5c, MovieS5 and MovieS6).

Thus, the Lokiarchaeal ESCRT-III/Vps4 system can deform free-standing-GUV membranes at the tens of micrometer scale, far exceeding the dimensions of archaeal cells. These observations extend the SLB results and suggest that this minimal archaeal ESCRT-III machinery has intrinsic large-scale membrane-remodelling activity.

Discussion

The ESCRT-III machinery drives membrane remodelling in eukaryotes and is present in several archaeal lineages, yet how minimal archaeal ESCRT systems assemble and function remains poorly understood[19,43]. Here, we reconstituted two ESCRT-III subunits and a single Vps4 ATPase from *Candidatus Lokiarchaeum* and show that this minimal system generates dynamic membrane-associated polymers and co-polymers spanning nanometre to micron scales. ESCRT-IIIA and ESCRT-IIIB form distinct assemblies, co-assemble into higher-order structures, and are differentially remodelled by Vps4. Thus, functional specialization, hierarchical assembly and selective ATPase-dependent regulation—central principles of eukaryotic ESCRT-III systems—are already present in a reduced archaeal machinery.

A striking feature of the Lokiarchaeal system is the difference in assembly scale between the two ESCRT-III subunits. ESCRT-IIIA forms micron-scale filaments, rings, bundles and branched networks on anionic membranes. These structures are substantially larger than the nanoscale spirals typically associated with canonical ESCRT-III membrane scission and are comparable to archaeal cell dimensions[44,45]. This suggests that ESCRT-IIIA can organize membrane surfaces over cellular length scales and may function as a membrane scaffold for large-scale processes such as cell division. By contrast, ESCRT-IIIB forms compact nanoscale spirals that are morphologically reminiscent of Snf7-like ESCRT-III assemblies[40], despite its phylogenetic placement within the “late” ESCRT-III group[23,46]. The coexistence of extended ESCRT-IIIA scaffolds and compact ESCRT-IIIB spirals suggests a division of labour in which the two subunits operate at distinct spatial scales.

Vps4 further differentiates the two proteins. ESCRT-IIIA assemblies are processively disassembled in an ATP-dependent manner, with Vps4 promoting filament shortening, ring constriction and loss of ordered polymer architecture. In contrast, ESCRT-IIIB spirals are not removed from the membrane by Vps4. Instead, Vps4 localizes to spiral edges and promotes their radial compression, eventually closing the inner orifice of the spirals. This shows that Lokiarchaeal Vps4 is not simply a general ESCRT-III disassembly factor, but can remodel different ESCRT-III polymers in subunit-specific ways. This asymmetric regulation correlates with the distinct predicted Vps4-interaction motifs of the two proteins,

with ESCRT-IIIA containing MIM1- and MIM2-like motifs and ESCRT-IIIB containing a MIM1-like element. Mutational analysis will be required to test whether these motifs directly determine the differential Vps4 response.

Order-dependent co-assembly of ESCRT-IIIA and ESCRT-IIIB reveals even more intriguing features of their spatial plasticity, supporting a hierarchical assembly pathway conceptually similar to eukaryotic ESCRT-III systems. This is particularly evident if ESCRT-IIIB is added to pre-assembled large-scale ESCRT-IIIA filaments and rings. Based on fluorescence and high-resolution EM images in Fig. 4a,c, we propose that the predicted N-terminal amphipathic h0 helix of ESCRT-IIIB may promote recruitment to ESCRT-IIIA-deformed membrane interfaces, where the two subunits co-assemble into spring-like polymers that accommodate their distinct curvature preferences (Fig. 5d). However, the resulting spring-like polymers differ from canonical ESCRT-III geometries in both scale and membrane orientation, a potential solution for the Lokiarchaeal system to access larger-scale modes of membrane organization (Fig. 5e).

Consistent with this idea, the reconstituted ESCRT-III/Vps4 machinery deforms free-standing GUV membranes, showing that the activities observed on supported bilayers can translate into large-scale membrane remodelling. In this context, we propose a speculative model in which this minimal system could be positioned and used as a division machinery, analogous to the Cdv ESCRT-like system from *S. acidocaldarius* (Fig. 5f). Whether these deformations proceed to membrane fission remains to be determined.

Asgard archaea are widely regarded as the closest known relatives of the archaeal lineage that gave rise to eukaryotes[47]. Thus the Lokiarchaeal ESCRT-III system studied here provides insight into the functional capabilities of an ancestral ESCRT machinery predating the emergence of complex endomembrane systems[48]. Recent reports of internal membrane compartmentalization in Asgard archaea further support the idea that such spatial organization can arise in archaeal cells[49]. Additionally, closely related archaea encoding both FtsZ/SepF and Cdv proteins have been shown to use an ESCRT-based cell-division machinery[50]. Collectively, these observations support a model in which eukaryotic ESCRT-III diversity emerged through expansion and refinement of pre-existing archaeal modules that were already functionally specialized.

This study relies on simplified phospholipid membranes rather than native archaeal lipids, which may influence ESCRT-III binding, polymer architecture and remodelling activity. Future work using archaeal lipid-based model membranes will be important for testing this machinery in a more native membrane environment. In addition, because the source organism is uncultured, *in vivo* validation of the proposed assembly pathway remains challenging. Advances in Asgard archaeal cultivation, imaging and heterologous expression should enable future tests of whether similar ESCRT-III structures form in cells and whether they contribute to division or intracellular membrane organization. Such efforts will not only advance understanding of ESCRT evolution but also provide broader insight into lipid–protein interactions across the lipid divide[51].

In summary, this work establishes a minimal Lokiarchaeal ESCRT-III/Vps4 system as a model for ancestral membrane-remodelling mechanisms. Two ESCRT-III subunits are sufficient to generate distinct homopolymers, order-dependent co-polymers and Vps4-responsive membrane-deforming assemblies. This minimal reconstitution provides a functional baseline for a modular ancestral ESCRT-III system, offering a framework to define general principles of membrane remodelling and clear targets for future in vivo studies. These findings reveal that complex ESCRT-III behaviours can emerge from a small number of archaeal components and suggest how ancestral ESCRT machineries may have contributed to the evolution of cellular membrane organization.

Secondary and tertiary structure prediction

Previously published Asgard ESCRT-III sequence datasets[23,52] were combined and manually curated. Secondary structure prediction was performed with a local installation of PSIPRED 4.0[53], a multiple sequence alignment (MSA) was generated with MAFFT v7.526[54] using flags "--localpair --maxiterate 1000", and a custom Python script was used to display the secondary structure prediction in MSA format. Interactions between the C-terminal regions of ESCRT-IIIs and the Vps4 MIT domain was predicted with AlphaFold3[55] using the online server and visualised with ChimeraX[56]. The N-terminal regions of ESCRT-III were analysed with the online tool PMIpred[57].

Protein expression and purification

Genes encoding Lokiarchaeal ESCRT-IIIA (Lokiarch_16760; CHMP4-7), ESCRT-IIIB (Lokiarch_37480; CHMP1-3), and Vps4 (Lokiarch_37470; VPS4) were codon-optimized for *Escherichia coli* expression and cloned into pCoofy38 vectors encoding N-terminal His–thioredoxin fusion tags with a 3C protease-cleavable site (Supplementary Data). To enable site-specific fluorescent labelling, a single cysteine residue was introduced at the C-terminus of ESCRT-IIIA and ESCRT-IIIB by site-directed mutagenesis. All constructs were verified by sequencing.

Proteins were expressed in *E. coli Rosetta* (DE3) cells. These were harvested, pooled and resuspended in lysis buffer (50 mM NaHPO, pH 7.5, 150 mM NaCl, 40 mM imidazole, 5 mM β-mercaptoethanol and protease inhibitors). Cells were lysed by sonication. His–Trx fusion proteins were purified by nickel-affinity chromatography, followed by cleavage of the Trx tag with 3C protease at 4°C overnight during dialysis, to remove imidazole. Reverse nickel-affinity chromatography was then performed to remove the cleaved tag. Fractions containing the protein were concentrated and loaded onto a Superdex 75 HiLoad column equilibrated in size-exclusion buffer (20 mM HEPES, pH 7.5, 250 mM NaCl, 2 mM dithiothreitol). Protein purity was assessed by mass spectrometry. Purified ESCRT-IIIA and ESCRT-IIIB containing a single C-terminal cysteine were concentrated and labelled with maleimide-functionalized fluorescent dyes (Alexa Fluor 488 or Alexa Fluor 565; Thermo Fisher Scientific) according to the manufacturer's instructions. Excess dye was removed with desalting columns. Concentrations were determined using the Bradford Assay (Bio-Rad, Hercules, CA, USA), flash-frozen in liquid nitrogen, and stored at − 80°C.

Dynamic light scattering

Dynamic light scattering (DLS) measurements were performed using a DynaPro Nanostar (Wyatt Technology) at 20°C after a 5-minute scattering signal. Proteins were diluted to final concentrations of 1 µM in assay buffer (20 mM HEPES, pH 7.5, 150 mM NaCl). Measurements were acquired with n ≥ 5 replicates (n = 15 measurements), and analyzed using the manufacturer's software to determine hydrodynamic radii.

Vps4 ATPase activity assay

ATP activity measurements were assessed using the commercially available malachite green assay (Malachite Green Phosphate Assay Kit; Sigma-Aldrich). Temperatures were set using a heating water bath. All experiments were performed using 250 nM Vps4 where background phosphate values were substracted. pH-range activity measurements reacted for 60 minutes in buffers containing 20 mM citrate buffer (for pH 5.4) or 20 mM HEPES, 150 mM NaCl, 2 mM $MgCl_2$, and 1 mM ATP, at a temperature of 42.5°C for pH values of 5.4, 6.8, 7.5 and 8.5 (n = 6). Temperature-range activity measurements reacted for 110 minutes in buffers containing 20 mM HEPES, pH 7.5, 150 mM NaCl, 2 mM $MgCl_2$, and 1 mM ATP, at temperatures of 22, 30, 40, 42.5, 45, 47.5, 50 and 60°C (n ≥ 3). We monitored the absorbance at 620 nm in transparent 96-well plate (Greiner) using Spark® Multimode microplate reader (TECAN), phosphate release was quantified using a standard curve.

Preparation of supported lipid bilayers

Small Unilamellar Vesicles (SUVs) were prepared from lipid mixtures (Lipid Mix 1) containing 1,2-Dioleoyl-sn-glycero-3-phosphocholin (DOPC), 1,2-dioleoyl-sn-glycero-3-phospho-L-serine (DOPS) and 1,2-dioleoyl-sn-glycero-3-phosphoethanolamine-ATTO655 (DOPE-ATTO655), dissolved in chloroform with a molar ratio of 59.95:40:0.05 (Avanti Polar Lipids), unless otherwise mentioned. Lipids dissolved in chloroform were dried under nitrogen gas, desiccated under vacuum for at least 1 hour, and rehydrated and vortexed for 1 minute in buffer (20 mM HEPES, pH 7.5, 150 mM NaCl) to a 1 mg/mL concentration. The lipid suspension was bath sonicated until the solution became clear, corresponding to SUV formation.

Glass coverslips were piranha cleaned for at least 30 minutes, rinsed with water, dried under nitrogen gas and oxygen plasma cleaned for 30 seconds. Silicon chambers were fixed on the glass coverslips (17 mm Ø 4-well Cat.No: 80466; Ibidi). Supported lipid bilayers (SLBs) were formed by pipetting SUVs in the chambers followed by addition of CaCl2 (2 mM final) to a final lipid concentration of 0.5 mg/mL for 10 min at room temperature. We extensively washed the newly formed SLBs to remove excess vesicles and CaCl2. Bilayer formation and homogeneity were verified by fluorescence microscopy.

Large Unilamellar Vesicle Preparation

Lipid mixes were dried under nitrogen gas and desiccated for at least one hour. The lipids were resuspended in 40°C heated buffer (HEPES 20 mM, pH7.5, 150 mM NaCl, 2 mM Mgcl2) and vortexed for a minute before going through 5 freeze thaw cycles in liquid nitrogen. LUVs were then extruded through a 200 nm filter (Avanti).

Giant Unilamellar Vesicle preparation

GUVs were prepared using Polyvinyl alcohol (Sigma-Aldrich MW 145000) assisted swelling[58]. Glass coverslips were cleaned with isopropanol and ddH2O, dired under nitrogen gas and PVA was spread on them, left to dry on a 60°C heating plate for 20 minutes. 10 µL of 4 $g.L^{-1}$ lipid mix was spread on the PVA and desiccated for 1 hour. We next added a swelling buffer (20 mM Hepes, pH 7.5, 50 mM NaCl, 200 mM sucrose) for 45 minutes and harvested GUVs by pipetting gently. 10 µL GUVs were then added to 90 µL volume of a balanced osmolarity buffer (20 mM Hepes, pH 7.5, 150 mM NaCl). This strategy offered stable and dense GUVs to image in time-lapse experiments.

In vitro reconstitution of ESCRT-III assemblies

Fluorescently labelled ESCRT-IIIA and/or ESCRT-IIIB were added to SLBs at mentioned concentrations in reaction buffer (20 mM HEPES, pH 7.5, 150 mM NaCl; 2 mM MgCl2, 2 mM ATP), except in ATP free experiments. After incubation (commonly 10 min, mentioned in figure legends), unbound protein was removed by gentle washing with 3 or more chamber volumes in experiments with sequential protein incubations. For Vps4-dependent remodeling assays, Vps4 and ATP (2 mM) were added to pre-assembled ESCRT-III structures.

Confocal fluorescence microscopy

Confocal imaging was performed using a Zeiss LSM 980 equipped with laser lines 488 (for Alexa488), 561 (for Alexa565) and 639 nm (for ATTO655); intensities were kept constant across experiments. Images were acquired (1024x1024 pixels) at room temperature using a C-Apochromat 40x/1.20 water-immersion objective (Carl Zeiss AG). Time-lapse imaging was performed with frame intervals of 5–20 seconds (512x512 pixels). Image analysis and intensity measurements were carried out using Fiji/ImageJ 1.54p. Line-scan intensity profiles were extracted from raw images and smoothed using a sliding average (± 1 pixel).

Atomic force microscopy

AFM imaging was acquired in liquid using a JPK Nanowizard 3 operated in QI mode with a PEAKFORCE-HIRS-F-B cantilever (Brücker AFM Probes, 0.12 N/m, tip radius 1–2 nm). SLBs with assembled ESCRT-III structures were imaged after rinsing with 5 chamber volumes for the mentioned incubation times. The set point force was 0.20 nN and a Z-range of 120 nm. Height images were flattened and analyzed using the manufacturer's software, Gwyddion v2.58 and Fiji/ImageJ 1.54p. Image processing involved plane leveling, polynomial row alignment, and conservative denoising.

Lipid monolayer preparation

Cryo-EM grids containing lipid monolayer were prepared in a polytetrafluoroethylene (PTFE) block containing 50 µl side-entry reservoirs, as described previously[59]. Briefly, the PTFE block was cleaned and prepared as described previously[60], and 48 ml buffer was added to each reservoir. The buffer contained

20 mM HEPES, pH 7.5, 150 mM NaCl, 2 mM MgCl2, 2 mM ATP. A freshly prepared lipid mixture in 9:1 (v/v) chloroform:methanol, at a lipid concentration of 0.01 mg ml^{-1}, was then carefully applied to the surface of the buffer in each reservoir. The lipid mixture comprised 60 mol% DOPC and 40 mol% DOPS. The PTFE block was incubated in a closed Petri dish over moistened filter paper for 60 min to allow formation of a lipid monolayer at the air–water interface. A Quantifoil R2/2 holey carbon grid, Au 200 mesh (Quantifoil Micro Tools GmbH), was then placed on each reservoir such that the grid floated on the buffer surface. A solution containing purified ESCRT-IIIA, ESCRT-IIIA or VPS4, either alone or in the indicated combinations, was then injected into each reservoir through the side-entry port. The final concentrations of ESCRT-IIIA, ESCRT-IIIA and VPS4 in the reservoirs were 20 μM, 20 μM and 5 μM, respectively. Where a protein was omitted from a 2D crystallisation experiment, an equivalent volume of buffer was added to the reservoir. Samples containing ESCRT-IIIA alone were incubated for a further 30 min. For sequential addition experiments containing ESCRT-IIIA and ESCRT-IIIA, the first protein was incubated for 30 min before addition of the second protein, followed by a further 30 min incubation. Experiments including VPS4 were incubated for 5 min after VPS4 protein addition. Grids were then carefully lifted from the reservoir surface and plunge-frozen using a Vitrobot Mark IV operated at 100% humidity, with a blot time of 4 s and a blot force of 3.

Cryo-electron microscopy

Grids containing ESCRT-IIIA or ESCRT-IIIA+ESCRT-IIIB were loaded into a Titan Krios G4i operated at 300 kV and equipped with a Falcon 4i direct electron detector with Selectris energy filter (Thermo Fisher Scientific). Grids containing ESCRT-IIIB+VPS4, ESCRT-IIIB+ESCRT-IIIA, or ESCRT-IIIA+VPS4 were loaded into a Talos Glacios cryo-transmission electron microscope (Thermo Fisher Scientific) operated at 200 kV and equipped with a Falcon 4i direct electron detector (Thermo Fisher Scientific). Micrographs were recorded as electron-event representation (EER) files[61], with a total electron dose of 40 e^{-} $Å^{-2}$, at a nominal magnification of ×92,000, corresponding to a pixel size of 1.22 Å per pixel. EER movies were rendered as an 8k x 8k grid, and further Fourier cropped into a 4k x 4k grid using RELION-4.0[62]. Movies were motion-corrected, dose-weighted and averaged using the MotionCor2 implementation in RELION-4.0[62,63]. Contrast transfer function parameters were estimated using CTFFIND4[64]. ESCRT-IIIA and ESCRT-IIIA+ESCRT-IIIB filaments were traced with filament picker in crYOLO[65], imported to cryoSPARC v4.0[66] and then extracted with a box size of 420 pixels and 600 pixels, respectively. The inter-box distance was set to 30 Å for ESCRT-IIIA, and 80 Å for ESCRT-IIIA+ESCRT-IIIB. Particles were Fourier-cropped to 128 pixels for ESCRT-IIIA and to 256 pixels for ESCRT-IIIA+ESCRT-IIIB, and subjected to several rounds of 2D classification. ESCRT-IIIB+VPS4 particles were picked as a regular grid of points spaced by 128 pixels, spanning coordinates 128–3968 × 128–3868 pixels within each 4k × 4k micrograph. Particles were then imported into cryoSPARC v4.0, extracted with a box size of 256 pixels and Fourier-cropped to 128 pixels. The particles were then subjected to two rounds of 2D classification.

Data analysis and statistics

Quantitative data are reported as mean ± s.d. unless otherwise indicated. The number of independent experiments or structures analyzed (n) is specified in the figure legends. Graphs and statistical analyses were generated using GraphPad Prism9.

Declarations

Data availability

All data are available in the text, figures, or supplementary information. All source data are provided as a Source Data file. Due to their large file size (>10 GB), the original image data files for in vitro screening and in vivo screening are available from the corresponding author upon request.

Acknowledgements

We thank the MPIB core facilities of protein production and biophysics for having helped with protein purification and biochemical characterization, in particular Yao Xiao and Anja Wehner. We also appreciate the work and help Michaela Schaper and Kerstin Röhrl provided for cloning and purifying proteins. We thank Svetozar Gavrilović who helped and assisted in acquiring AFM data. We are grateful for the constructive feedback and interactions within our department that assisted this project.

Funding

Open access funding was provided by the Max Planck Society. This work was supported by the Deutsche Forschungsgemeinschaft (DFG) through the DIP programme (project number 509481440).

Author information

Authors and Affiliations

Department of Cell and Molecular Biophysics, Max Planck Institute of Biochemistry, Am Klopferspitz 18, Martinsried, 82152 Munich, Germany.

Henry Živković, Béla Frohn and Petra Schwille.

Department of Cell and Virus Structure, Max Planck Institute of Biochemistry, Am Klopferspitz 18, Martinsried, 82152 Munich, Germany.

Dominik Hrebík, Margot Riggi and John A.G. Briggs.

Department of Structural Cell Biology, Max Planck Institute of Biochemistry, Am Klopferspitz 18, Martinsried, 82152 Munich, Germany.

Jérôme Basquin.

Department of Structural Cell Biology, Max Planck Institute of Biochemistry, Am Klopferspitz 18, Martinsried, 82152 Munich, Germany.

Contributions

H.Z. and P.S. conceived the study. H.Z. designed and performed the in vitro reconstitution experiments, confocal microscopy, AFM experiments, and data analysis. H.Z. and D.H. performed cryo-electron microscopy experiments and D.H. analyzed and processed data. H.Z. and J.B. performed protein purification and biochemical characterization. B.P.F. performed computational analysis. M.R. and H.Z. prepared illustrations. H.Z. and P.S. wrote the manuscript with input from all authors. P.S and J.A.G.B obtained funding and supervised the project.

Corresponding author

Correspondence to Petra Schwille.

Ethics declarations

Competing interests

The authors declare no competing interests.

References

1. Carlton JG, Baum B (2023) Roles of ESCRT-III polymers in cell division across the tree of life. Curr Opin Cell Biol 85:102274
2. Banjade S, Zhu L, Jorgensen JR, Suzuki SW, Emr SD (2022) Recruitment and organization of ESCRT-0 and ubiquitinated cargo via condensation. Sci Adv 8:eabm5149
3. Liu J, Kang R, Tang D (2021) ESCRT-III-mediated membrane repair in cell death and tumor resistance. Cancer Gene Ther 28:1–4
4. Enkavi G, Javanainen M, Kulig W, Róg T, Vattulainen I (2019) Multiscale Simulations of Biological Membranes: The Challenge To Understand Biological Phenomena in a Living Substance. Chem Rev 119:5607–5774
5. Hurley JH, Coyne AN, Miączyńska M, Stenmark H (2025) The expanding repertoire of ESCRT functions in cell biology and disease. Nature 642:877–888
6. Avalos-Padilla Y et al (2021) The ESCRT-III machinery participates in the production of extracellular vesicles and protein export during Plasmodium falciparum infection. PLoS Pathog 17:e1009455
7. Carlton JG, Agromayor M, Martin-Serrano J (2008) Differential requirements for Alix and ESCRT-III in cytokinesis and HIV-1 release. PNAS 105:10541–10546
8. Sprenger S et al (2021) Rules for the Self-Assembly of ESCRT-III on Endosomes. 02.19.431979 https://www.biorxiv.org/content/10.1101/

2021.02.19.431979v1
(2021) doi:10.1101/2021.02.19.431979

9. Pfitzner A-K, Zivkovic H, Humbert F, Roux A (2022) Vps60 initiates formation of alternative membrane-bound ESCRT-III filaments. 02.16.480668 Preprint at https://doi.org/10.1101/2022.02.16.480668 (2022)
10. Pfitzner A-K et al (2020) An ESCRT-III Polymerization Sequence Drives Membrane Deformation and Fission. Cell 182:1140–1155e18
11. McCullough J et al (2015) Structure and membrane remodeling activity of ESCRT-III helical polymers. Science 350:1548–1551
12. Babst M (2011) MVB vesicle formation: ESCRT-dependent, ESCRT-independent and everything in between. Curr Opin Cell Biol 23:452–457
13. Christ L et al (2016) ALIX and ESCRT-I/II function as parallel ESCRT-III recruiters in cytokinetic abscission. J Cell Biol 212:499–513
14. Prescher J et al (2015) Super-Resolution Imaging of ESCRT-Proteins at HIV-1 Assembly Sites. PLoS Pathog 11:e1004677
15. Harel S (2021) *Characterization of Individual HIV-1 Budding Event Using Ultra-Fast Atomic Force Microscopy Reveals a Multiplexed Role for VPS4*. http://biorxiv.org/lookup/doi/10.1101/2021.12.12.472262 doi:10.1101/2021.12.12.472262
16. Pust S, Brech A, Wegner CS, Stenmark H, Haglund K (2022) *Vesicle-Mediated Transport of ALIX and ESCRT-III to the Intercellular Bridge during Cytokinesis*. http://biorxiv.org/lookup/doi/10.1101/2022.11.22.517322 10.1101/2022.11.22.517322
17. Goliand I et al (2018) Resolving ESCRT-III Spirals at the Intercellular Bridge of Dividing Cells Using 3D STORM. Cell Rep 24:1756–1764
18. Vietri M, Radulovic M, Stenmark H (2020) The many functions of ESCRTs. Nat Rev Mol Cell Biol 21:25–42
19. Hatano T et al (2022) Asgard archaea shed light on the evolutionary origins of the eukaryotic ubiquitin-ESCRT machinery. Nat Commun 13:3398
20. Spang A et al (2015) Complex archaea that bridge the gap between prokaryotes and eukaryotes. Nature 521:173–179
21. Eme L et al (2023) Inference and reconstruction of the heimdallarchaeial ancestry of eukaryotes. Nature 1–8. 10.1038/s41586-023-06186-2
22. Tobiasson V, Luo J, Wolf YI, Koonin EV (2026) Dominant contribution of Asgard archaea to eukaryogenesis. Nature 650:141–149
23. Souza DP et al (2025) Asgard archaea reveal the conserved principles of ESCRT-III membrane remodeling. Sci Adv 11:eads5255
24. Melnikov N (2022) *Asgard ESCRT-IIIs Assemble into Helical Filaments in the Presence of DNA and Remodel Eukaryotic Membranes*. http://biorxiv.org/lookup/doi/10.1101/2022.09.07.506706

doi:10.1101/2022.09.07.506706

25. Lu Z et al (2020) Coevolution of Eukaryote-like Vps4 and ESCRT-III Subunits in the Asgard Archaea. *mBio* 11. 10.1128/mbio.00417 - 20
26. Risa GT et al (2020) The proteasome controls ESCRT-III–mediated cell division in an archaeon. Science 369
27. Härtel T, Schwille P (2014) ESCRT-III mediated cell division in Sulfolobus acidocaldarius – a reconstitution perspective. Front Microbiol 5:257
28. Blanch Jover A, De Franceschi N, Fenel D, Weissenhorn W, Dekker C (2022) The archaeal division protein CdvB1 assembles into polymers that are depolymerized by CdvC. FEBS Lett 596:958–969
29. Pulschen AA et al (2020) Live Imaging of a Hyperthermophilic Archaeon Reveals Distinct Roles for Two ESCRT-III Homologs in Ensuring a Robust and Symmetric Division. Curr Biol 30:2852–2859e4
30. Babst M, Katzmann DJ, Estepa-Sabal EJ, Meerloo T, Emr SD (2002) Escrt-III: An endosome-associated heterooligomeric protein complex required for mvb sorting. Dev Cell 3:271–282
31. Williams TA, Low HH (2025) The evolution and mechanism of bacterial and archaeal ESCRT-III-like systems. Curr Opin Struct Biol 93:103111
32. Wenzel DM (2022) *Comprehensive Analysis of the Human ESCRT-III-MIT Domain Interactome Reveals New Cofactors for Cytokinetic Abscission*. http://biorxiv.org/lookup/doi/10.1101/2022.02.09.477148 doi:10.1101/2022.02.09.477148
33. Alonso Y, Adell M, Teis D (2011) Assembly and disassembly of the ESCRT-III membrane scission complex. FEBS Lett 585:3191–3196
34. Sciskala B, Kölling R (2013) Interaction Maps of the Saccharomyces cerevisiae ESCRT-III Protein Snf7. Eukaryot Cell 12:1538–1546
35. Scott A et al (2005) Structural and mechanistic studies of VPS4 proteins. EMBO J 24:3658–3669
36. Ramirez-Diaz DA et al (2018) Treadmilling analysis reveals new insights into dynamic FtsZ ring architecture. PLoS Biol 16:e2004845
37. Wisanpitayakorn P, Mickolajczyk KJ, Hancock WO, Vidali L, Tüzel E (2022) Measurement of the persistence length of cytoskeletal filaments using curvature distributions. Biophys J 121:1813–1822
38. Ramirez-Diaz DA et al (2021) FtsZ induces membrane deformations via torsional stress upon GTP hydrolysis. Nat Commun 12:3310
39. Naskar S (2023) *Mechanism for Vipp1 Spiral Formation, Ring Biogenesis and Membrane Repair*. http://biorxiv.org/lookup/doi/10.1101/2023.09.26.559607 doi:10.1101/2023.09.26.559607
40. Jukic N, Perrino AP, Humbert F, Roux A, Scheuring S (2022) Snf7 spirals sense and alter membrane curvature. Nat Commun 13:2174
41. Bertin A et al (2020) Human ESCRT-III polymers assemble on positively curved membranes and induce helical membrane tube formation. Nat Commun 11:2663

42. Chiaruttini N et al (2015) Relaxation of Loaded ESCRT-III Spiral Springs Drives Membrane Deformation. Cell 163:866–879
43. McCullough J, Frost A, Sundquist WI, Structures (2018) Functions, and Dynamics of ESCRT-III/Vps4 Membrane Remodeling and Fission Complexes. Annu Rev Cell Dev Biol 34:85–109
44. Salcher MM et al (2020) Visualization of Lokiarchaeia and Heimdallarchaeia (Asgardarchaeota) by Fluorescence In Situ Hybridization and Catalyzed Reporter Deposition (CARD-FISH). *mSphere* 5, e00686-20
45. Imachi H et al (2020) Isolation of an archaeon at the prokaryote–eukaryote interface. Nature 577:519–525
46. Liu J et al A relay race of ESCRT-III paralogs drives cell division in a hyperthermophilic archaeon. mBio 16, e00991–e00924
47. Spang A et al (2015) Complex archaea that bridge the gap between prokaryotes and eukaryotes. Nature 521:173–179
48. Field MC, Dacks JB (2009) First and last ancestors: reconstructing evolution of the endomembrane system with ESCRTs, vesicle coat proteins, and nuclear pore complexes. Curr Opin Cell Biol 21:4–13
49. MacLeod FI et al (2025) An Asgard archaeon with internal membrane compartments. 11.06.686947 Preprint at https://doi.org/10.1101/2025.11.06.686947 (2025)
50. Pelve EA et al (2011) Cdv-based cell division and cell cycle organization in the thaumarchaeon Nitrosopumilus maritimus. Mol Microbiol 82:555–566
51. Mondal S, Kumar S, Sankaranarayanan R (2025) An Integrative View on Multiple Lipid Divide Events as Hallmarks of Distinct Evolutionary Transitions. Biochemistry 64:4487–4497
52. Frohn BP, Härtel T, Cox J, Schwille P (2022) Tracing back variations in archaeal ESCRT-based cell division to protein domain architectures. PLoS ONE 17:e0266395
53. McGuffin LJ, Bryson K, Jones DT (2000) The PSIPRED protein structure prediction server. Bioinformatics 16:404–405
54. Katoh K, Standley DM (2013) MAFFT Multiple Sequence Alignment Software Version 7: Improvements in Performance and Usability. Mol Biol Evol 30:772–780
55. Abramson J et al (2024) Accurate structure prediction of biomolecular interactions with AlphaFold 3. Nature 630:493–500
56. Meng EC et al (2023) UCSF ChimeraX: Tools for structure building and analysis. Protein Sci 32:e4792
57. van Hilten N et al (2024) PMIpred: a physics-informed web server for quantitative protein–membrane interaction prediction. Bioinformatics 40:btae069
58. Weinberger A et al (2013) Gel-Assisted Formation of Giant Unilamellar Vesicles. Biophys J 105:154–164
59. Stacey JCV et al (2025) The conserved HIV-1 spacer peptide 2 triggers matrix lattice maturation. Nature 640:258–264

60. Truong CD, Williams DR, Zhu M, Wang JC-Y, Chiu P-L (2021) Sample Preparation using a Lipid Monolayer Method for Electron Crystallographic Studies. J Vis Exp. https://doi.org/10.3791/63015
61. Guo H et al (2020) Electron-event representation data enable efficient cryoEM file storage with full preservation of spatial and temporal resolution. IUCrJ 7:860–869
62. Kimanius D, Dong L, Sharov G, Nakane T, Scheres SH (2021) W. New tools for automated cryo-EM single-particle analysis in RELION-4.0. Biochem J 478:4169–4185
63. Zheng SQ et al (2017) MotionCor2: anisotropic correction of beam-induced motion for improved cryo-electron microscopy. Nat Methods 14:331–332
64. Rohou A, Grigorieff N (2015) CTFFIND4: Fast and accurate defocus estimation from electron micrographs. J Struct Biol 192:216–221
65. Wagner T et al (2019) SPHIRE-crYOLO is a fast and accurate fully automated particle picker for cryo-EM. Commun Biol 2:218
66. Punjani A, Rubinstein JL, Fleet DJ, Brubaker MA (2017) cryoSPARC: algorithms for rapid unsupervised cryo-EM structure determination. Nat Methods 14:290–296

Figures

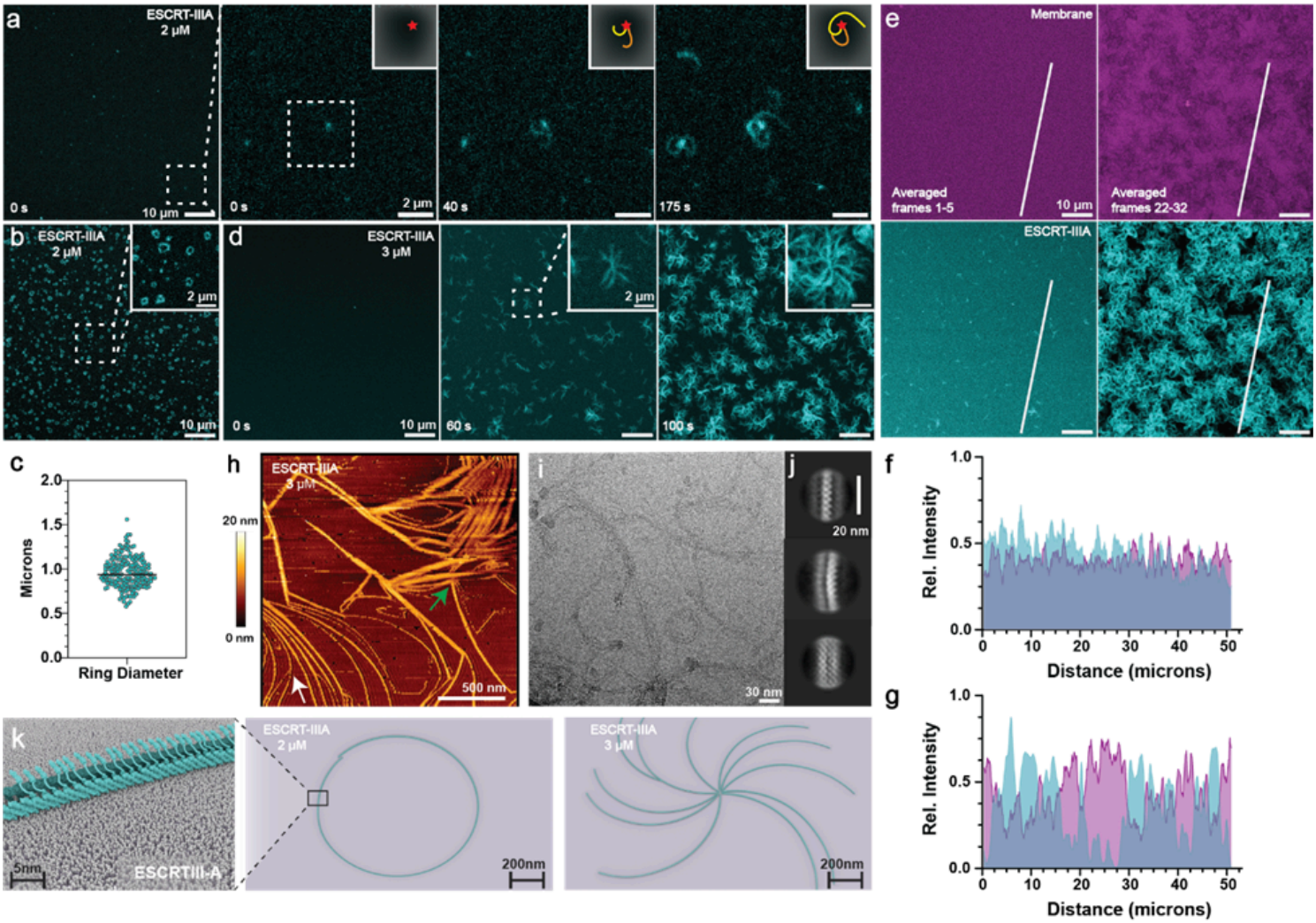


Figure 1

ESCRT-IIIA assembles into filaments and rings on negatively charged bilayers

a, Confocal fluorescence images of a time-lapse in which ESCRT-IIIA–Alexa488 (cyan) is added at 2 µM on supported lipid bilayers composed of DOPC:DOPS:DOPE-ATTO655(59.95:40:0.05 mol%). Colored stars highlight nucleation sites and lines indicate representative filaments. **b**, Same as (a), with ESCRT-IIIA rings formed at 2 µM after 10 minutes incubation. **c**, Plotted measurements of ring diameters from two different days including (c) (mean 0.96 ± s.d. 0.17; n = 191). **d**, Fluorescence images of a time-lapse with ESCRT-IIIA (3 µM) filaments on SLBs. **e**, Averaged images of the time-lapse images from (a). Left panels show the membrane channel(magenta) and right panels the ESCRT-IIIA channel. Top panels represent averaged images of frames 1-5 (from 40 s before to 40 s after ESCRT-IIIA addition), and bottom panels represent averaged images of frames 22–32 (400–600 s after ESCRT-IIIA addition). White lines indicate positions used for intensity profiles measured in (f,g). **f**, Line-scan intensity profiles measured along the indicated lines in (e) (before filament formation). ESCRT-IIIA fluorescence is shown in blue and membrane fluorescence in magenta. Profiles were smoothed using a sliding average (± 1 pixel). **g**, Line-scan intensity profiles as in (f), measured from the bottom panels of (e) (after filament formation). **h**, AFM height image of ESCRT-IIIA assemblies (3 µM; 30 min) on supported lipid bilayers as in (a), imaged after rinsing the chambers. **i**, Cryo-electron micrograph of ESCRT-IIIA filaments (20 µM; 30 min) assembled on lipid monolayers of the same composition as in (a). **j**, Two-dimensional class averages showing the protofilament organization. **k**, Close-up and larger-scale schematic illustrating ESCRT-IIIA filaments (cyan) growing into clockwise rings (left) orbranching (right) from an initial nucleation centre on a lipid membrane surface. Representative images of n ≥ 3 (a, b, c, e and i) and n = 2 (h) independent experiments.

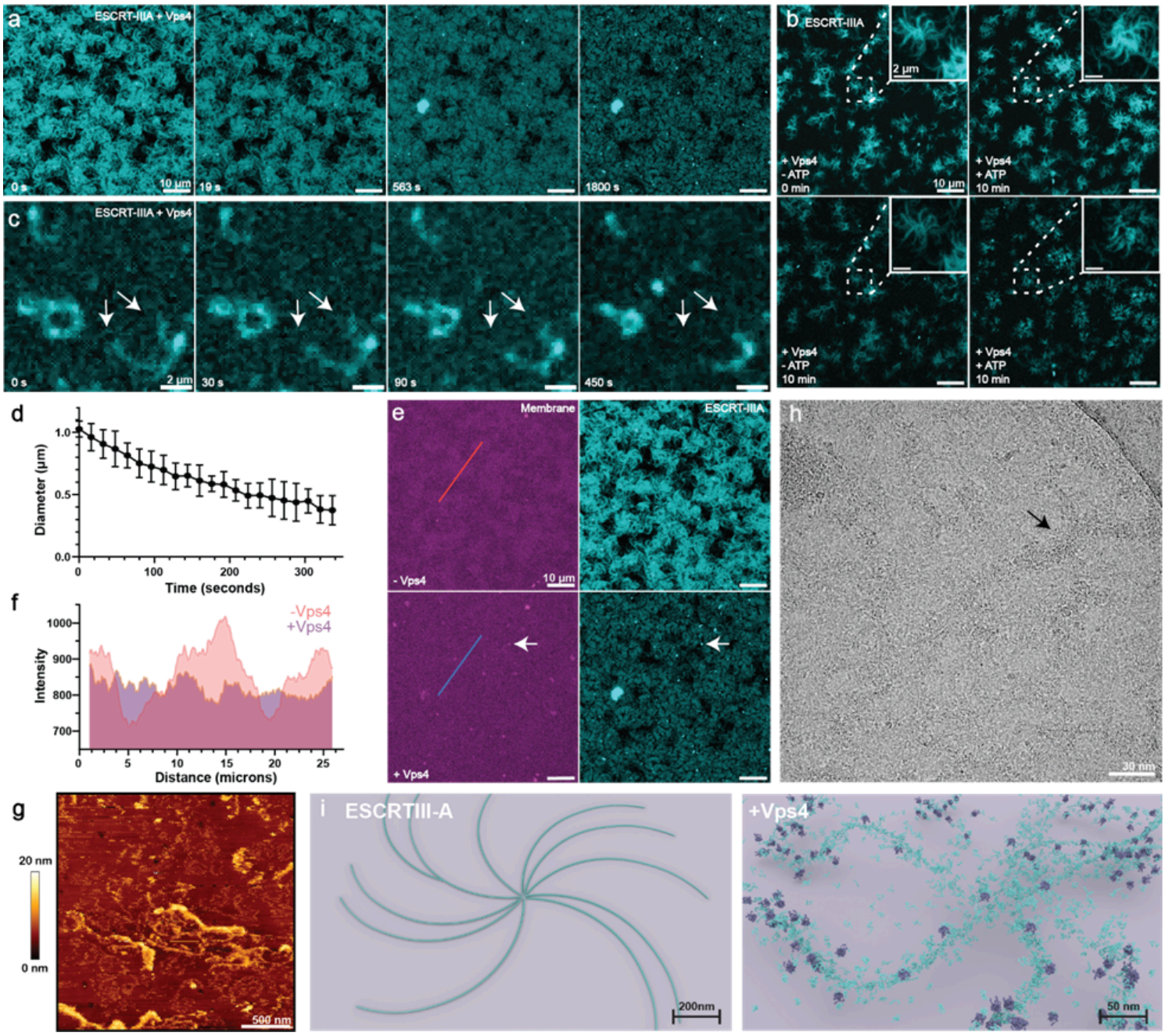


Figure 2

Vps4 disassembles ESCRT-IIIA filaments and rings

a, Confocal fluorescence images of a time-lapse, where ESCRT-IIIA–Alexa488 (3 µM; cyan) is prepared with supported lipid bilayers composed of DOPC:DOPS:DOPE-ATTO655 (59.95:40:0.05 mol%), rinsed out and incubated with Vps4 (3 µM). **b**, Same as (a), with ESCRT-IIIA and Vps4 at 3 µM. Left panels are 0 and 10 min after addition of Vps4 without ATP, right panels issued from an experiment with 2 mM ATP. **c**, ESCRT-IIIA (2 µM) rings rinsed out before addition of Vps4 at 3 µM. Rings are constricted and arrows indicate filaments shortening. **d**, Average ring diameter over time from experiments performed as in (c) (n = 4). **e**, Confocal images from (a). Left panels show the membrane channel (magenta) and right panels the ESCRT-IIIA channel. Top panels are before Vps4 (3 µM) addition and bottom panels after

addition. Arrows show colocalizing defects of ESCRT-IIIA and membrane emerging after Vps4 addition. Colored lines indicate positions used for intensity profiles in (f). **f**, Line-scan intensity profiles of the membrane channel before (red) and after Vps4 addition (blue). Profiles were smoothed using a sliding average (± 1 pixel). **g**, AFM height image of ESCRT-IIIA assemblies (3 µM; 30 min) washed and incubated with Vps4 (2 µM, 30 min) on supported lipid bilayers. **h**, Cryo-electron micrograph of ESCRT-IIIA filaments (20 µM; 30 min) assembled and incubated with Vps4 (2 µM; 30 min) on lipid monolayers. Arrow indicates disassembled or aggregated protein following a filament-like pattern. **i**, Schematic illustrating ESCRT-IIIA filaments (cyan, left) branched from an initial nucleation centre on a lipid membrane surface. Upon Vps4 addition (purple), disassembly preferentially occurs at filament extremities. Representative images of n ≥ 3 (a, b, c, d) and n = 2 (g,h) independent experiments.

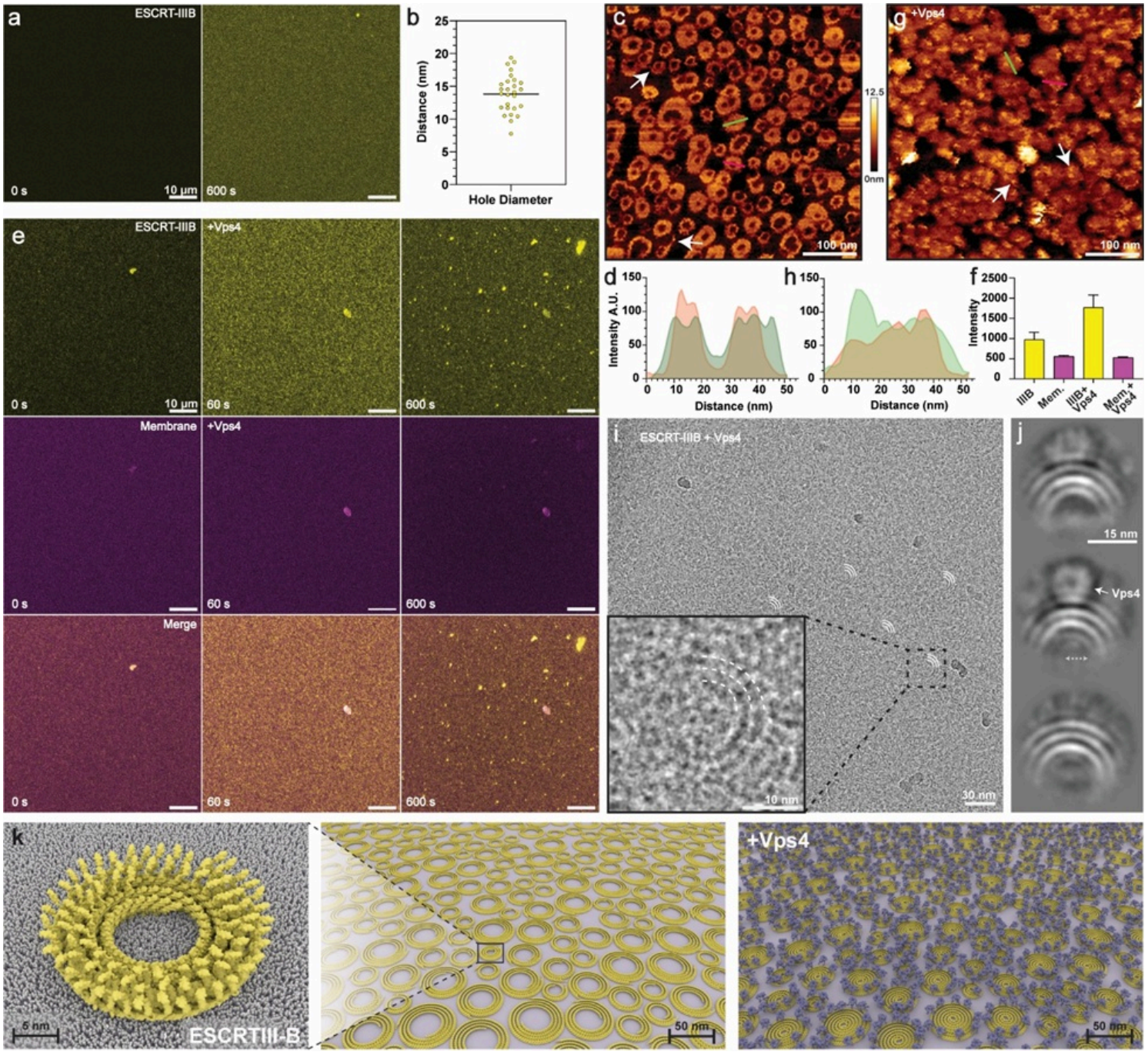


Figure 3

ESCRT-IIIB forms Snf7-like spirals on negatively charged membranes

a, Confocal fluorescence images of ESCRT-IIIB–Alexa565 (yellow) at 500 nM added to supported lipid bilayers composed of DOPC:DOPS:DOPE-ATTO655(59.95:40:0.05 mol%). **b**, Plotted measurements of ring diameters from two different days including (c) (mean 13.8 ± s.d. 2.7 nm; n = 30). **c**, AFM height image of ESCRT-IIIB assemblies (2 μM; 30 min) on supported lipid bilayers as in (a), imaged after rinsing out. Arrows indicate protein filaments diverging from spirals. Green and red lines illustrate the intensity profiles used in (c). **d**, Line-scan intensity profiles measured along the indicated lines in (b). Profiles were smoothed using a sliding average (± 1 pixel). They emphasize dual- and triple-stranded spirals (red and green), with central holes measuring a mean 13.8 ± s.d. 2.7 nm (n = 30).
e, Same as (a). ESCRT-IIIB (500 nM) was washed and unlabeled Vps4 (2 μM) was added at 60 s. Protein channel, membrane channel (magenta), and merge are shown from top to bottom. **f**, Histogram of whole-image averaged absolute fluorescence intensities. Conditions were measured for ESCRT-IIIB and membrane fluorescence before and after Vps4 (2 μM) addition (n = 3). **g**, AFM height image of ESCRT-IIIB assemblies (2 μM; 30 min) washed and incubated with Vps4 (2 μM; 30 min) on supported lipid bilayers. Arrows indicate densities appearing upon Vps4 addition. Green and red lines illustrate the intensity profiles used in (g). **h**, Line-scan intensity profiles measured along the indicated lines in (f). Profiles were smoothed using a sliding average (± 1 pixel). They emphasize that strands and central holes are less discernible than in (c). **i**, Cryo-electron micrograph of ESCRT-IIIB (20 μM; 30 min) assembled and incubated with Vps4 (2 μM; 30 min) on lipid monolayers. White quarter-rings follow spiral filaments to aid visualization. **j**, Two-dimensional class averages showing tight, regular ESCRT-IIIB spirals. Arrow points to Vps4 hexamers. Double-headed arrow in the middle image represents the inner cavity. Representative images of n ≥ 3 (a and d) and n = 2 (b, f and h) independent experiments. **k**, Close-up and larger-scale schematic illustrating ESCRT-IIIB spirals (yellow) forming and propagating across a lipid membrane surface. Spirals are multi-stranded, irregular, and contain a central hole. Upon Vps4 addition, spirals condense toward their centres and strands gain regularity through tightening.

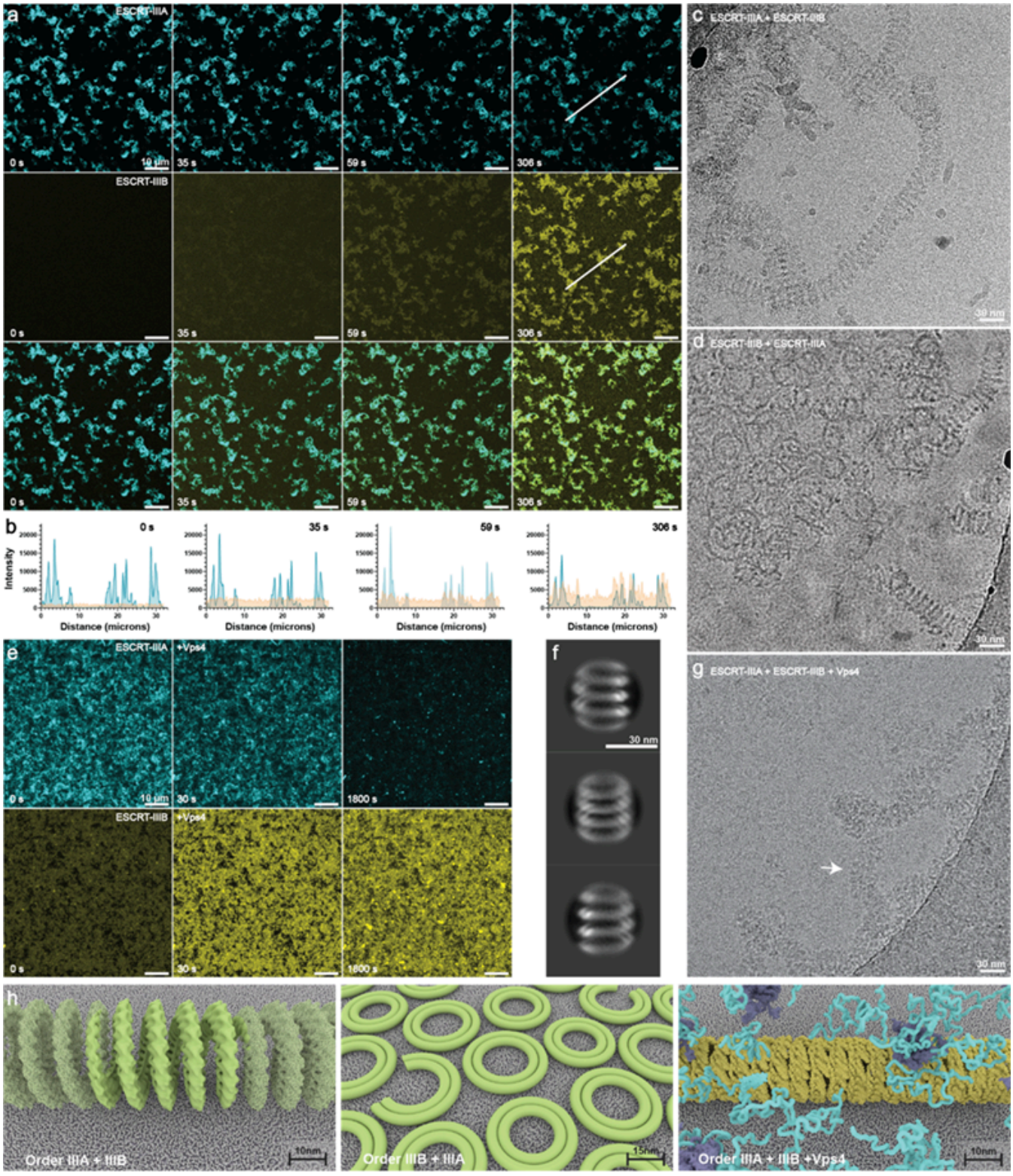


Figure 4

ESCRT-IIIA recruits ESCRT-IIIB and forms spring-like structures

a, Confocal fluorescence images of ESCRT-IIIA–Alexa488 (2 µM; top; cyan) rinsed out before adding ESCRT-IIIB–Alexa565 (500 nM; middle; yellow) and the merge of both channels (bottom) on supported lipid bilayers composed of DOPC:DOPS:DOPE-ATTO655 (59.95:40:0.05 mol%). Lines illustrate the

intensity profiles used in (b). **b**, Line-scan intensity profiles measured along the indicated lines in (a). Each profile corresponds to the time point of the image above in (a). Profiles were smoothed using a sliding average (± 1 pixel). **c**, Cryo-electron micrograph of ESCRT-IIIA (20 µM; 30 min) assembled and then incubated with ESCRT-IIIB (20 µM; 30 min) on lipid monolayers. The spring on this micrograph is close to 460 nm long. **d**, The same experiment as in (c) with the order inverted (ESCRT-IIIB followed by ESCRT-IIIA) is shown below. Ring-like intermediates or uncoiled structures are observed. **e**, Confocal fluorescence images of ESCRT-IIIA–Alexa488 (3 µM; top), ESCRT-IIIB (750 nM; middle), and merge (bottom) sequentially incubated and washed before adding Vps4 (2 µM) on supported lipid bilayers. **f**, Two-dimensional class averages of spring-like structures. **g**, Cryo-electron micrograph of ESCRT-IIIA (20 µM; 30 min) and ESCRT-IIIB (20 µM; 30 min) sequentially incubated and washed before adding Vps4 (2 µM; 15 min) on lipid monolayers. Arrow points to remnants of spring-like structures. **h**, Spring-like structures (green, left) formed co-dependently in theESCRT-IIIA and ESCRT-IIIB sequential order. These span without continuous contact with the lipid membrane. Intermediate circular structures observed from ESCRT-IIIB and ESCRT-IIIA sequential order (green, middle). Upon Vps4 addition(right), ESCRT-III proteins (-IIIA cyan, -IIIB yellow) are differentially regulated according to their individual behaviours in the presence of Vps4(purple). Representative images of n ≥ 3 (a and d) and n = 2 (c and f) independent experiments.

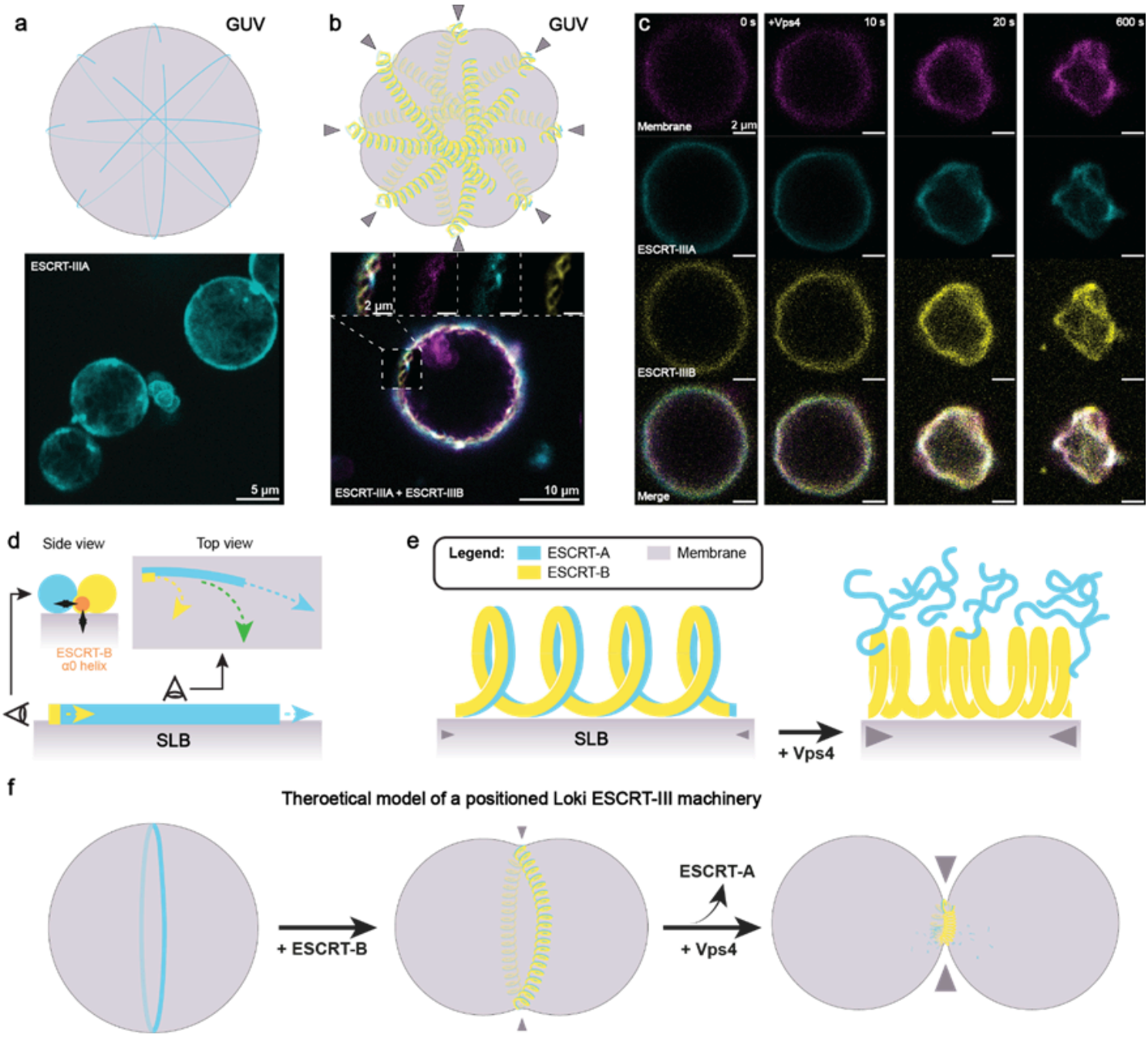


Figure 5

Large-scale Lokiarchaeal ESCRT-III-mediated GUV constriction and hypothetical models

a Confocal fluorescence image of a ESCRT-IIIA–Alexa488 (cyan) added at 3 µM to GUVs composed of DOPC:DOPS:DOPE-ATTO655 (59.95:40:0.05 mol%). Above is a schematic illustration of the confocal image result with ESCRT-IIIA. **b** Confocal fluorescence image of a ESCRT-IIIA–Alexa488 (cyan) added at 3 µM, followed by ESCRT-IIIB at 500 nM to GUVs. Above is a schematic illustration of the confocal image result with ESCRT-IIIA. **c** Confocal fluorescence images of a GUV time-lapse experiment where membrane, ESCRT-IIIA–Alexa488 (cyan), ESCRT-IIIB-Alexa565 and merge channels are displayed from top to bottom. Vps4 is added at 2 µM in the presence of ATP. **d**, Hypothetical model: On the left, a side-view of ESCRT-IIIB (yellow) lateral binding at the ESCRT-IIIA-membrane interface (cyan-grey respectively).

Additionally, a top-view of the mechanical compromise found (green arrow) when intrinsic curvatures of ESCRT-IIIA (cyan arrow) and ESCRT-IIIB (yellow arrow) associate. **e**, Hypothetical model: On the left, a resulting spring-like structure. On the right, asymmetrical Vps4 regulation of ESCRT-IIIA being removed, and ESCRT-IIIB condensed and supercoiling. Here, supplementary ESCRT-IIIB membrane-anchoring points are generated. **f**, Hypothetical model of how Loki ESCRT-III system could be used for cell division, with a sequential ESCRT-IIIA ring positioning (left), ESCRT-IIIB reorganization of the ring into a spring-like ring (middle) and finally, a progressive constriction of a cell (right) relying on principles described in (e).

Supplementary Files

This is a list of supplementary files associated with this preprint. Click to download.

- SupplementaryInformation.pdf
- MovieS42uM3A3uMvps410minmedianblur0.81.avi
- MovieS23uM3A10min.avi
- MovieS33uM3A10minmembraneChannel.avi
- MovieS52uMvps4noATP10min.avi
- MovieS62uMVps4ATP2mM10min.avi
- MovieS12uM3A10min.avi